Volumetric directional optical coherence tomography

SHUIBIN NI,[1,2] ⬤ SHANJIDA KHAN,[1,2] THANH-TIN P. NGUYEN,[1] RINGO NG,[3] BRANDON J. LUJAN,[1] OU TAN,[1] DAVID HUANG,[1,2] AND YIFAN JIAN[1,2,*]

[1]*Casey Eye Institute, Oregon Health & Science University, Portland, Oregon 97239, USA*
[2]*Department of Biomedical Engineering, Oregon Health & Science University, Portland, Oregon 97239, USA*
[3]*School of Engineering Science, Simon Fraser University, Burnaby, British Columbia V5A 1S6, Canada*
[*]*jian@ohsu.edu*

Abstract: Photoreceptor loss and resultant thinning of the outer nuclear layer (ONL) is an important pathological feature of retinal degenerations and may serve as a useful imaging biomarker for age-related macular degeneration. However, the demarcation between the ONL and the adjacent Henle's fiber layer (HFL) is difficult to visualize with standard optical coherence tomography (OCT). A dedicated OCT system that can precisely control and continuously and synchronously update the imaging beam entry points during scanning has not been realized yet. In this paper, we introduce a novel imaging technology, Volumetric Directional OCT (VD-OCT), which can dynamically adjust the incident beam on the pupil without manual adjustment during a volumetric OCT scan. We also implement a customized spoke-circular scanning pattern to observe the appearance of HFL with sufficient optical contrast in continuous cross-sectional scans through the entire volume. The application of VD-OCT for retinal imaging to exploit directional reflectivity properties of tissue layers has the potential to allow for early identification of retinal diseases.

1. Introduction

Age-related macular degeneration (AMD) is the leading cause of blindness in the elderly population [1]. Geographic atrophy (GA), the advanced stage of the non-exudative (dry) form of AMD, is characterized by the loss of the photoreceptors, the retinal pigment epithelium (RPE), and the choriocapillaris [2]. There is currently no effective treatment for GA [1]. Therefore, the detection of pathological biomarkers for staging of AMD before the development of GA is critical to the development of effective therapies and clinical prognostication. Several imaging techniques, including color fundus photography, fundus autofluorescence (FAF), and optical coherence tomography (OCT), have been applied to detect areas of GA [3–6]. Histopathological work has supported the view that photoreceptor degeneration occurs early in some AMD cases [7]. Thus, photoreceptor degeneration and resultant thinning of the outer nuclear layer (ONL), which contains the nuclei of photoreceptor cells, is an important clinical feature of AMD [8]. However, it is challenging to demarcate the boundary between the ONL and the neighboring Henle's fiber layer (HFL), which consists of Müller cells and cone photoreceptor axons [8]. These fibers run obliquely from the cell bodies outward to their synapses, and are typically not visualized on standard OCT images because most of the backscattered signal from HFL is reflected away from the detector and blends in with the hypo-reflective ONL [9]. The grouping of HFL and ONL confounds ONL thickness measurements, as the thickness of these layers is not proportional [10].

Therefore, measuring HFL thickness is essential for accurate evaluation of ONL thickness in OCT. Lujan *et al.* extended on the initial observation of HFL visibility by developing a technique using multiple pupil entry positions to provide better optical contrast to differentiate

HFL and ONL called Directional OCT (D-OCT) [9,10]. Otani *et al.* also sought to position the measurement beam perpendicular to HFL to enhance visualization [11]. Oscar *et al.* demonstrated a pupil tracking OCT system to automatically control the OCT beam pupil entry position which enabled reliable visualization of HFL on cross-sectional OCT scans [12]. Wartak *et al.* used a multi-channel OCT system to acquire three OCT B-scans from three separate directions simultaneously [13]. Using these research prototype systems, it was possible to measure the true HFL and ONL thickness within the macular region by acquiring several OCT volumes at different pupil entry positions. However, its clinical utility was lessened by long imaging sessions and patient fixation requirements. Moreover, these volumes taken at different angles needed to be registered and averaged with complex image processing techniques. A dedicated OCT system that can delineate ONL and HFL in a single volume has not yet been demonstrated.

Due to the constraints of hardware configuration and specialized scanning protocols, the advantages of directional OCT imaging technology have not yet been fully realized. In this study, we proposed a novel Volumetric Directional OCT (VD-OCT) prototype that incorporates two sets of optical scanners in the OCT sample arm to synchronously scan the imaging beam on both pupil and retina planes. We also implemented a novel customized image acquisition protocol that we call the spoke-circular scanning pattern to further harness the advantages of the prototype. To the best of our knowledge, this is the first dedicated prototype that can acquire and differentiate ONL and HFL with sufficient optical contrast within the macular region in a single volume. The investigation of ONL and HFL independently might have potential to provide an in-depth understanding of the pathological process of progression from normal retina to advanced AMD.

2. Methods

2.1. VD-OCT system design

The schematic diagram of the VD-OCT system is shown in Fig. 1. This system is based on a spectral domain OCT engine. The light source was a superluminescent diode (SLD) centered at 840 nm, with a 90 nm bandwidth (M-D-840-HP, Superlum, Ireland), and provided an axial resolution of 3.45 μm in air. The light from the source was guided into one of the fiber coupler's ports (Gould Fiber Optics, USA) and split into the sample (20%) and reference (80%) arms. The detection of the OCT interferogram (purple dashed box in Fig. 1) consisted of a high-speed spectrometer (Cobra-S 800, Wasatch photonics Inc., USA) integrated with a 2048-pixel camera (Octoplus, Teledyne e2v Ltd., UK). The camera operated at a line rate of 240 kHz and with a 10-bit bit-depth mode. A PCIe frame grabber (PCIe-1437, National Instrumental Corp., USA) was used to capture the recorded interferometric fringes. The imaging system triggering, synchronization, and scanning waveform generation were provided by a multifunctional DAQ (PCIe-6353, National Instrumental Corp., USA).

The sample arm of our VD-OCT system was comprised of a deformable mirror (DM) (DMP40-F01, Thorlabs Inc., USA), a paired galvanometer scanning mirror (simply as "Galvo" in the following discussions) (Saturn-5B, Pangolin Laser Systems Inc., USA) that was conjugated to the pupil plane, a fast steering mirror (FSM) (OIM5002, Optics In Motion LLC, USA) that was conjugated to the retina plane, and several telescope relay lenses. The red dashed box in Fig. 1 shows the beam pathway when only the Galvo was scanning (as in a regular OCT system). The trajectory of the beam motion by the scanning of both Galvo and FSM synchronously was shown in the cyan dashed box on the bottom left corner in Fig. 1. The red dot lines represent the envelope of all Galvo scanning angles for different FSM scanning configurations. The scanners' synchronization will be discussed in detail in the following "image acquisition protocols" section.

To aid with system alignment and monitoring the beam scanning within the pupil, a pupil camera (FFY-U3-04S2M-S, Teledyne FLIR LLC, USA) was embedded into the sample arm, as shown in the red and cyan dashed boxes in Fig. 1. A 5.5-inch display was installed to serve as a fixation target. A dichroic mirror (Chroma Technology Corp., USA) was also mounted to couple
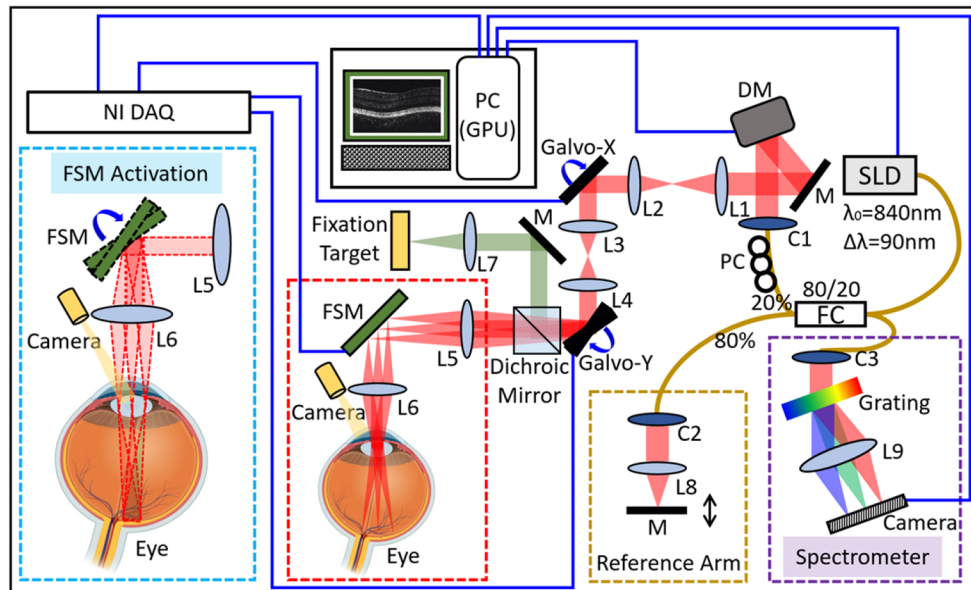
Fig. 1. Schematic diagram of the VD-OCT system. The purple dashed box on the bottom right corner illustrates the spectrometer combined with a 2048-pixel camera. The dark-yellow dashed box on the bottom center shows the schematic of the reference arm. The red dashed box on the bottom center illustrates the regular OCT galvanometer scanning system. The cyan dashed box on the bottom left corner demonstrates the VD-OCT system when both the galvanometer scanner and FSM are activated synchronously. The red dot lines represent the beam envelope with different scanning angle configurations of FSM. SLD: superluminescent diode; M: mirror; DM: deformable mirror; L1-L9: lens; C1-C3: collimator; Galvo-X/Galvo-Y: the fast/slow axis of galvanometer scanner; FSM: fast steering mirror; NI DAQ: multifunctional data acquisition and control card; PC: polarization controller; FC: fiber coupler; GPU: graphics processing unit.

the beam from the fixation target to the main optical axis. For *in vivo* human retinal imaging, the incident power on the subject's cornea was set to less than 0.9 mW, which is lower than the safe ocular laser exposure limit by the American National Standards Institute (ANSI) Z80.36-2016 standards [14].

2.2. Optical design

The optical design of the sample arm is shown in Fig. 2. The sample arm was constructed using off-the-shelf lenses (Thorlabs Inc., USA) listed in Table 1. Using OpticStudio (Zemax LLC, USA), the optical layout was simulated and the design was optimized by minimizing the imaging beam wander on the pupil plane and root mean square (RMS) spot radius on the retina plane. The beam was collimated by a reflective collimator (RC12APC-P01, Thorlabs Inc., USA) and reflected off two alignment mirrors before reaching the piezoelectric DM. The DM, which was comprised of 40 independently controlled actuators, was placed on the pupil conjugate plane before the Galvo to correct for defocus and astigmatism. This design was adapted from our sensorless AO-OCT system [15]. The diameter of beam was first reduced to 4.3 mm after passing through the first telescope [L1 and L2 in Fig. 2(a)] in the system. It was then scanned across the X-axis and Y-axis by a pair of Galvo. The paired scanners were separated by a set of achromatic lenses with 4f configuration [L3 and L4 in Fig. 2(a)] without magnification. In previous work, we have shown that the separated Galvo significantly reduced the vignetting artifacts and minimized

the imaging beam wander on the pupil plane [16]. After the Galvo, the combination of the L5 and L6 in Fig. 2(a) served as the second telescope with a magnifying power of 0.39× to further reduce the beam size to 1.5 mm on the pupil plane, yielding a spot size of 11.9 μm (1/e² diameter) on the retinal plane. A two-inch FSM that has two axes of mirror motion as a result of its mobile magnet design, was positioned on the retinal conjugate plane in between the second telescope to synchronously scan along with the Galvo.
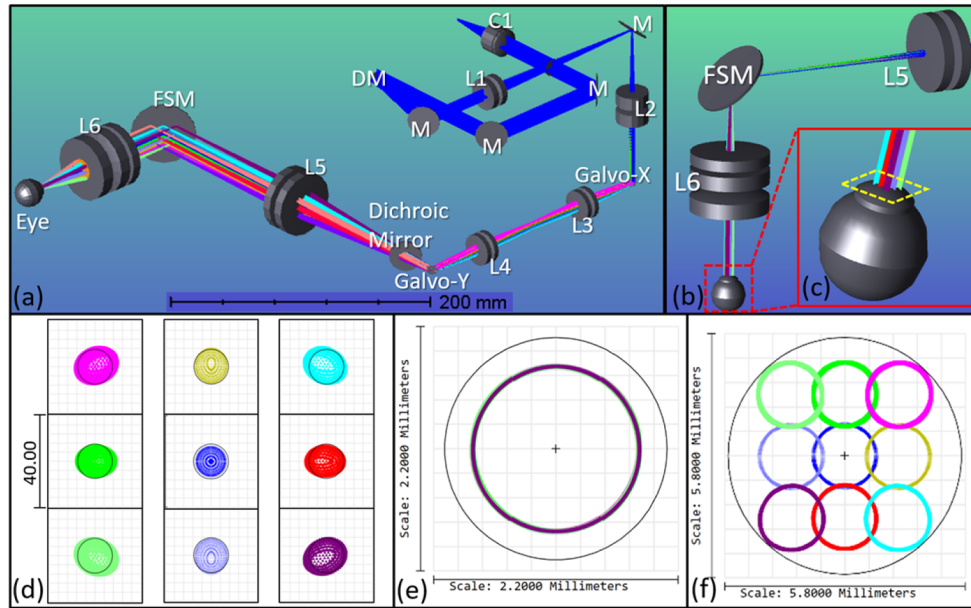

Fig. 2. (a) Isometric view of the sample arm optical simulation in OpticStudio. (b). Ray trace simulation when the FSM is scanning, corresponding to the cyan dashed box in Fig. 1. (c) Zoomed-in inset of the beam trajectory in the eye model. (d). The spot diagrams with 10° FOV centered at the fovea of an eye model. The radius of Airy Disk is 7.56 μm and shown by black circle in spot diagrams. (e). Footprint diagram with different Galvo scanning angle configurations on the pupil plane. (f) Footprint diagram with different FSM scanning angle configurations on the pupil plane.

Table 1. List of optical lenses for the sample arm

Item [Fig. 2(a)]	Part Number[a]	Quantity	Focal length (mm)	Diameter (mm)
L1	AC254-300-B	2	300	25.4
L2	AC254-125-B	2	125	25.4
L3	AC254-100-B	2	100	25.4
L4	AC254-100-B	2	100	25.4
L5	AC508-300-B	2	300	50.8
L6	AC508-300-B	1	300	50.8
	AC508-150-B	1	150	50.8
	AC508-100-B	1	100	50.8

[a]All the listed part numbers were off-the-shelf lenses from the Thorlabs Inc., USA

The minimization of beam wandering on the pupil was imperative for the successful measurement of the angle-dependent optical reflectivity. The FSM scanned in two-axis resulting in a

beam trajectory on the pupil plane shown in Fig. 2(f). The working distance (from the last lens surface of the sample arm to the subject's cornea) of the system was 42.7 mm, which was sufficient for imaging adults.

2.3. Mechanical design and system assembly

The optimized optical simulation of the sample arm was utilized to specify the locations of the optical components. Mechanical design for the sample arm was developed in the CAD software (SolidWorks, Dassault Systèmes, France) and is shown in Fig. 3(a). The sample arm was built on a compact two-layer structure with the center of gravity concentrated near the center, avoiding mechanical instability during the alignment process. The top layer included the collimator (C1), the DM, a telescope (L1-L2), and several tuning mirrors. The mirrors were mounted on flexure mirror mounts (MFM-100, Newport Corp., USA) that can accommodate tip and tilt using set screws, and the mounts were assembled to the system with custom-made aluminum brackets. All these components were fitted on an 8" × 8" × 0.5" aluminum breadboard (MB8, Thorlabs Inc., USA), and the remaining components were placed on a 12" × 18" × 0.5" aluminum breadboard (MB1218, Thorlabs Inc., USA) as the bottom layer. The two-layer structure was mounted on a custom three-axis alignment platform. The horizontal movement of the platform was manually controlled by a joystick with a ball cage, and the height adjustments were made using a stepper motor stage (X-LRQ-E Series, Zaber Technologies Inc., Canada).
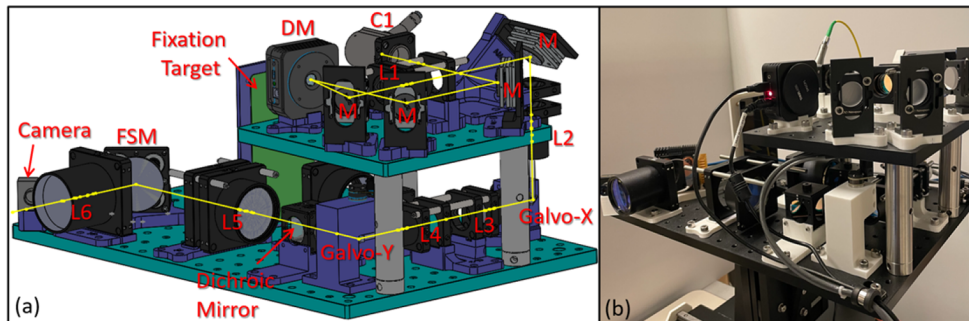

Fig. 3. (a) 3D mechanical layout of the sample arm. (b) Photograph of the fully assembled sample arm.

2.4. Image acquisition protocol

In order to observe morphology of HFL within the macula region effectively, we designed an imaging acquisition protocol called spoke-circular scanning pattern. Spoke-circular scanning pattern was composed of spoke scans on the retina and a synchronous circular scan on the pupil. The retinal spoke scan consisted of a series of equiangular spokes centered at the fovea, spanning the entire 360°. The spoke scan on the retina was analogous to the clock hand motion with an anticlockwise direction. When the retinal scan was at 9 o'clock direction, the pupil beam entry point was at the opposite 3 o'clock position. When the retinal scan was at 12 o'clock direction, the pupil beam entry point was at the opposite 6 o'clock position. Each spoke on the retina had a corresponding incident beam entry position on the pupil. When the spoke scan on the retina was moving in an anticlockwise direction radially, the beam on the pupil was moving in an anticlockwise direction in a circle. Note that the period of the pupil circular scan in the spoke-circular scanning pattern was the same as each volume acquisition time.

　　Figures 4(a) and (c) indicate two kinds of scanner driving signal waveform with normalized amplitude, which were applied to FSM and Galvo synchronously in the spoke-circular scanning

pattern. When the channels of FSM were applied with the driving signal waveforms in Fig. 4(a), the FSM trajectory was obtained, as shown in Fig. 4(b). And the same is true of the Galvo trajectory [Figs. 4(c) and 4(d)]. The illustrations were under-sampled for simplicity. The amplitude of both scanners could be adjusted in our software to meet the requirements with respect to scanning size on the retina and pupil. The retinal spoke scan consisted of 600 A-scans per B-scan, 2 repeated B-scans at each radial location, and 600 B-scans (300 different spokes) per volume. Each volume acquisition time was 1.5 seconds. Spokes on the retinal [Fig. 4(f)] and incident beam entry position on the pupil [Fig. 4(e)] were selected every 45° in a scanning cycle to demonstrate the effect of spoke-circular scan in practice. Synchronization with the two sets of optical scanners was critical when applying the spoke-circular scanning pattern. The emphasized configuration of phase opposition and synchronization ensured that the appearance of HFL in every cross-sectional image would have high directional reflectivity.
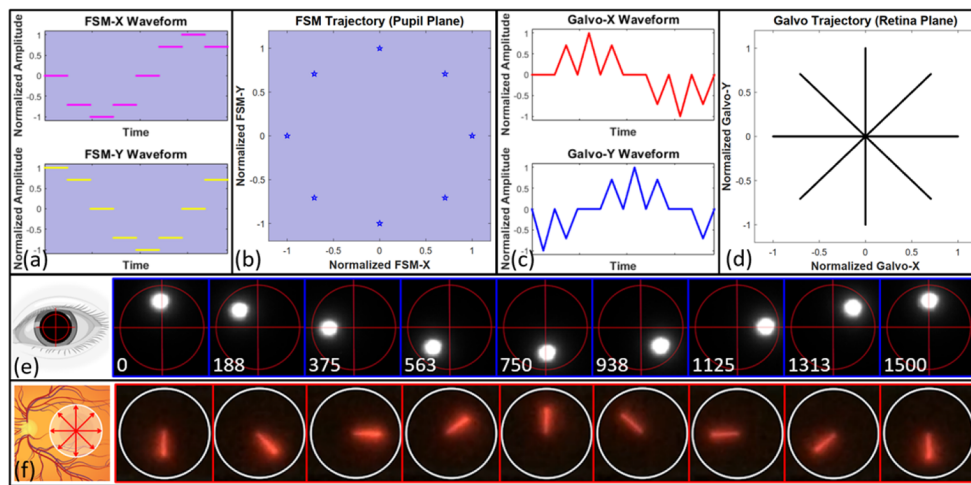

Fig. 4. (a) Drive signal waveforms of the fast and slow axis of FSM in the spoke-circular scanning pattern. (b) FSM trajectory on the pupil plane. (c) Drive signal waveforms of the fast and slow axis of Galvo in the spoke-circular scanning pattern. The waveforms for both FSM and Galvo were under-sampled along the angular axis for clarity (600 A-scans per B-scan, 2 B-scans per BM-scan, 16 B-scans per volume). (d) Galvo trajectory on the retina plane. (e) The snapshots from the video recording the imaging beam trajectory on the pupil plane. The time intervals of a period were shown in the left bottom of each snapshot (unit: ms). Red circle and crosshair were inserted into video snapshots manually to illustrate the trajectory of the imaging beam. (f) The snapshots from the video recording the entire B-scan on the retinal plane. The infrared light was visualized by the NIR detector card (VRC5, Thorlabs Inc., USA).

2.5. Software operation and data visualization

OCT images were acquired and processed by our custom written graphics processing unit (GPU) accelerated software OCTViewer to provide real-time visualization of OCT images, which allows assessing the image quality immediately [17,18]. Customized imaging acquisition scanning pattern was generated in the MATLAB (MathWorks Inc., USA) and then uploaded to OCTViewer. These synchronized scanning patterns were converted to voltage control waveforms by the NI DAQ and then sent to the drivers of the FSM and Galvo.

The imaging session started in high-speed mode with a 10-Hz volume rate to quickly align to the area of interest. Once the target area was located, a hill-climbing algorithm for aberration

correction was performed in ~2 seconds based on the brightness of *en face* images [19]. After optimization, subjects were allowed to blink before acquiring images. Subsequently, we switched to the customized acquisition mode with the spoke-circular scanning pattern, which continuously captured volumes every 1.5 seconds. Prior to acquiring a volume, the entry position of the incident beam on the pupil was fine-tuned in both horizontal and vertical directions with the aid of the integrated pupil camera to ensure that the scanning trajectory of the incident beam was not out of the pupil.

Raw OCT interferometric data was saved during the image session and processed with regular OCT image processing procedure in custom written MATLAB script. All the cross-sectional scans in the same volume were registered against the first cross-sectional scan to remove motion artifacts. The processed OCT volumes were manually segmented for quantitative analysis of retinal layer thickness. The primary layers of interest were outer plexiform layer (OPL), HFL, and ONL. Therefore, the retina layers were segmented on the top of OPL, the boundary between HFL and ONL (or the boundary between OPL and HFL in the regular spoke scanning pattern), and the top of IS/OS.

3. Results

Five subjects were recruited from the Casey Eye Institute at the Oregon Health & Science University (OHSU) and provided written informed consent prior to initiating the study. The research was approved by the Institutional Review Board/Ethics Committee of OHSU in accordance with the Declaration of Helsinki. In this study, four subjects had myopic spherical errors (−5.0D ~ −3.0D) and no subject reported any known ocular diseases. To ensure all the beams were able to pass through the pupil, three subjects were dilated with cyclopentolate hydrochloride and phenylephrine hydrochloride to achieve an adequate pupil size. Care was provided to adjust both the height of the chair and the chin rest position to ensure each subject was kept in a comfortable position during the imaging session. All subjects were successfully imaged by the VD-OCT prototype, and the following results were representative of images acquired in these sessions.

In the regular spoke scanning pattern, the scans on the retina were a series of cross-sectional scans with equiangular interval, which resembled bicycle spokes [Fig. 4(d) or Fig. 5(c)]; meanwhile, the incident beam for all spokes went through the center of the pupil [Fig. 5(a)]. In the spoke-circular scanning pattern the scans on the retina were the same as the regular scanning pattern [Fig. 5(c)], however each spoke had a specific corresponding incident beam entry position on the pupil [Fig. 5(d)]. This allowed us to precisely control the incident beam at an appropriate angle to generate sufficient optical contrast for the HFL in every cross-sectional scan. These moving entry positions formed a complete circle on the pupil. A series of cross-sectional OCT retinal images obtained by the spoke-circular scanning pattern [Fig. 5(e)] were compared to the cross-sectional OCT images acquired by a regular spoke scanning pattern [Fig. 5(b)]. It is obvious that when scanned with the spoke-circular pattern, the thickness of the combined layers of OPL and HFL [Fig. 5(e)] increased owing to the appearance of HFL (simply as "OPL + HFL" in the following discussion), in comparison with single layer of OPL in regular spoke scanning pattern [Fig. 5(b)]. Cross-sectional images from the regular spoke scanning pattern have higher signal-to-noise ratio (SNR) compared to the images from the spoke-circular scanning pattern. The reduced SNR could be due to the beam vignetting and/or optical aberrations when scanning with the spoke-circular scanning pattern.

The OPL and ONL thickness measurements were obtained separately from the regular spoke scanning pattern and spoke-circular scanning pattern. In the regular spoke scan pattern, HFL was not visible and often grouped together with ONL [red arrows in Fig. 5(b)], and in the spoke-circular scanning pattern, HFL was visible, however grouped together with OPL instead [cyan arrows in Fig. 5(e)]. By measuring the thickness of OPL + HFL in the spoke-circular

Fig. 5. (a) Incident beam entry positions in the regular spoke scanning pattern. (b) Eight selected cross-sectional scans (every 45° interval in a scanning cycle) acquired by the regular spoke scanning pattern. Red arrows indicate the combined layers of ONL and HFL. Orange arrows indicate the OPL. (c) Illustration of retinal spoke scan. (d) Corresponding incident beam entry positions in the spoke-circular scanning pattern. (e) Eight selected cross-sectional scans (every 45° interval in a scanning cycle) acquired by the spoke-circular scanning pattern. Yellow arrows indicate the ONL. Cyan arrows indicate the combined layers of OPL and HFL. Scale bars in (b) and (e) are 300 µm (horizontally) and 100 µm (vertically).

scanning pattern [Fig. 6(a)-①] and the thickness of OPL only in the regular spoke scanning pattern [Fig. 6(a)-②], we could infer the thickness of HFL. The mean thickness value and standard deviation of OPL, HFL and ONL were calculated and plotted respectively in Fig. 6(b). As the eccentricity increased, the HFL was approximately twice the thickness of OPL. The result was consistent with Otani *el al.*'s finding that the outer two-thirds of OPL + HFL showed hyper-reflective property [11]. To compare the OPL (or OPL + HFL) thickness across the entire parafovea region, volumetric remapping was implemented by cubic scattered data interpolation in post processing (Visualization 1 and Visualization 2). The volumetric OPL (or OPL + HFL) thickness heat maps were also calculated and plotted in Fig. 7(c) (Regular spoke scanning pattern) and Fig. 7(d) (Spoke-circular scanning pattern). The difference of thickness was apparent in
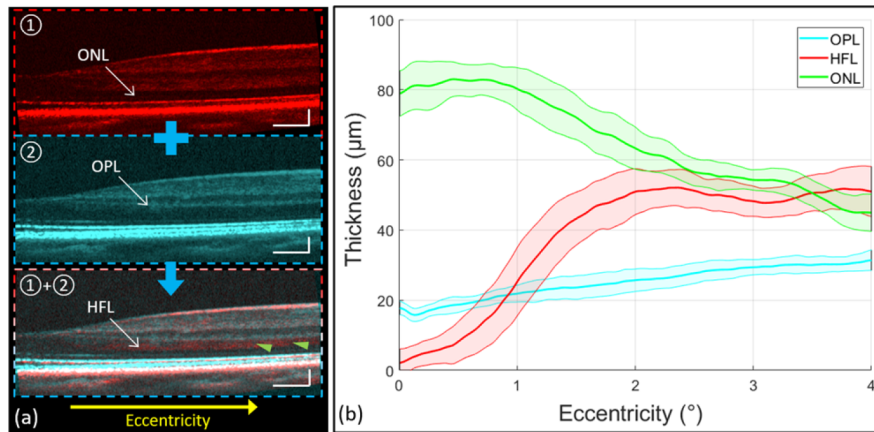
Fig. 6. (a) Selected cross-sectional scans acquired by the spoke-circular scanning pattern ("①" with red color coded), the regular spoke scanning pattern ("②" with cyan color coded), and the registration and average of the above cross-sectional scans to emphasize HFL (pointed by the green arrows in "①+②"). (b) The retinal layer thickness along various retinal eccentricities. The mean value (solid lines) and standard deviation (upper and lower bounds of the shaded areas around the solid lines) of each layer were calculated from 300 different spokes in the volume. The green line is the mean of ONL thickness ["①" in (a)] and the cyan line is the mean of OPL thickness ["②" in (a)] measured in images by the regular spoke scanning pattern. The red line is the mean of HFL ["①+②" in (a)] thickness through the registration of cross-sectional scans acquired by both scanning patterns. Scale bars in (a) are 300 μm (horizontally) and 100 μm (vertically).
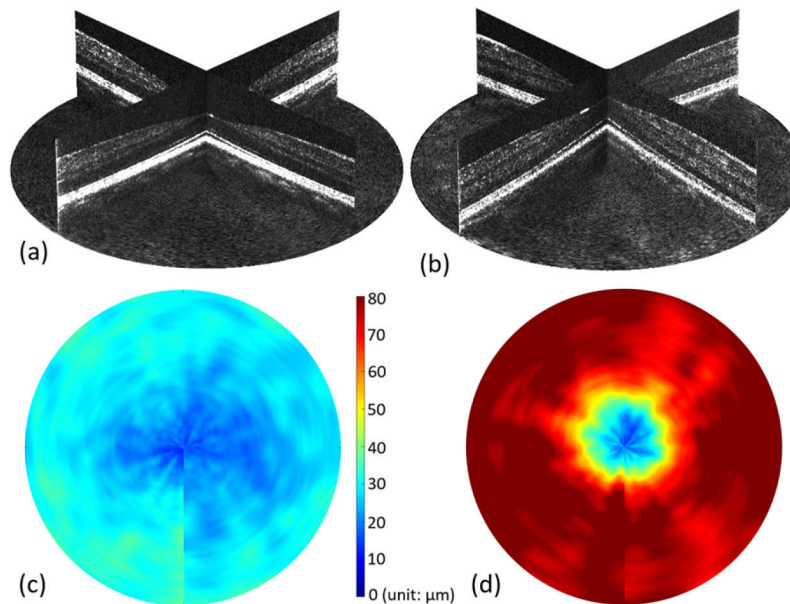

Fig. 7. (a) Screen capture of 3D volume rendering (Visualization 1) of cross-sectional scans acquired by the regular spoke scanning pattern. (b) Screen capture of 3D volume rendering (Visualization 2) of cross-sectional scans acquired by the spoke-circular scanning pattern. (c) The OPL thickness heat map centered at the fovea of the remapping volume acquired by the regular spoke scanning pattern. (d) The OPL + HFL thickness heat map centered at the fovea of the remapping volume acquired by the spoke-circular scanning pattern.

comparison with the heat maps. HFL became hyper-reflective in the macular region and increased the thickness of OPL + HFL while applying the spoke-circular scanning pattern.

4.   Discussion

The preceding results show that ONL and HFL within the macula region could be independently revealed efficiently in a single volume with the integration of the VD-OCT prototype and the customized scanning pattern. As mentioned above, the HFL contains obliquely oriented photoreceptor axons and Müller cell processes [7]. VD-OCT takes advantage of the directional reflectivity of this orientation which reflects the incidence beam at different angles differently. The enhancement of the optical contrast at some specific incidence beam entry position enables the visualization of HFL on the cross-sectional scans. The quantitative analysis for the OPL/OPL + HFL across the parafovea region rather than several individual cross-sectional OCT images might facilitate the investigation of pathological biomarkers. Future studies that seek to identify baseline thickness and subsequent thinning of ONL in AMD and other retinal diseases would benefit from these measurements. Thickness of the ONL is the gold-standard biomarker for retinal degenerations in small animals, as it precisely measures the survival of viable photoreceptor cells [20,21]. However, the same approach in humans and non-human primates, which possess a fovea, is confounded by the presence of the HFL [9,11]. The oblique orientation of photoreceptor axons in HFL is intrinsic to the foveal pit, where the cells of the inner nuclear layer (INL) are displaced eccentrically from the photoreceptors of the ONL. This displacement is accomplished developmentally by elongation of the HFL radially [22]. These fibers are long cylindrical elements and are highly directionally reflective [23] and indistinguishable from ONL on standard OCT, thus preventing their independent measurements. Consequently, the ONL and HFL are often grouped together in clinical studies, without independent analysis of the contributions of each layer leading to a loss of precision and accuracy in measuring the integrity of the photoreceptor cell bodies [24,25]. Change in the ONL thickness has been reported in *ex vivo* studies in normal aging [26–28], as well as in AMD [29]. There has previously been a contradiction between ONL measured by OCT imaging and by histological sectioning in non-human primates [30]. If HFL thickness increases but the ONL is thinning with age, as demonstrated by Curcio *et al.* [8], their combined thicknesses may appear relatively constant despite significant opposite changes in the thickness of each layer. Therefore, the ability to measure ONL and HFL thickness independently may lead to improved understanding of the retinal degeneration occurring in AMD, as well as the longitudinal effects of therapeutic interventions. Furthermore, conclusions regarding the extent of retinal damage and remodeling cannot accurately be made without distinguishing the ONL from HFL, as these layers may respond differently to cellular injury over time.

Besides HFL, other retinal layers, such as RNFL, IS/OS, and RPE were also found highly sensitive to the incident beam orientation and exhibited directional scattering properties [31–33]. In principle, the proposed VD-OCT prototype and spoke-circular scanning pattern could be extended to implement the observation of other retinal layers with directionally reflective properties. If necessary, it is also flexible to generate other scanning patterns for the detection of those layers according to their characteristics.

Despite providing a volumetric analysis for the retinal layer with directionally reflective property, there are some limitations of the VD-OCT prototype. First, both misalignment and eye motion would contribute to the vignetting artifacts. An integrated pupil tracking system could facilitate the alignment process and reduce the vignetting artifacts [12,34]. In addition, although the center wavelength in the OCT engine is near infrared (840 nm), it is still visible to the naked eye. Therefore, the subject's fixation during scanning is unconsciously affected as it moves with the scanning beam. Using an OCT imaging system with a center wavelength of 1060 nm, which is completely invisible, might address this issue [16]. Furthermore, the retinal layers were

segmented manually in this study because the current segmentation algorithm was not optimized to segment the boundary between OPL and HFL. We have previously demonstrated real-time OCT segmentation software using deep learning and GPU computing that can segment eight retinal layer boundaries [35]. Adapting this software for the VD-OCT to automatically segment and further analyze the accurate thickness of ONL is meaningful in the future. It is also worth noting that the adaptive optics (AO) module in our VD-OCT was not critical in visualizing or acquiring the directional contrast.

5.   Conclusion

A novel VD-OCT prototype with two sets of optical scanners was built in this study to investigate the effects of the different incident beam entry points on the pupil on the optical contrast of HFL. The proposed VD-OCT prototype provides a more reliable and efficient approach to clearly distinguish the structure with directional reflectivity in the peripapillary and the macular region in comparison with the conventional D-OCT based on the existing clinical commercial systems. Our novel imaging technology has the potential to reveal a more complete understanding of pathological biomarkers and track AMD progression for future clinical studies.

Disclosures. David Huang: Optovue Inc. (F, I, P, R). Brandon J. Lujan: Direction OCT, UC Berkeley (I). Yifan Jian: Seymour Vision (O). These potential conflicts of interest have been reviewed and managed by OHSU. Other authors declare no relevant conflicts of interest related to this article.

Data availability. Data underlying the results presented in this paper are not publicly available at this time but may be obtained from the authors upon reasonable request.

References

1. D. S. Friedman, B. J. O'Colmain, B. Muñoz, S. C. Tomany, C. McCarty, P. T. V. M. DeJong, B. Nemesure, P. Mitchell, J. Kempen, and N. Congdon, "Prevalence of age-related macular degeneration in the united States," Arch. Ophthalmol. **25**(4), 564–572 (1941).
2. F. G. Holz, E. C. Strauss, S. Schmitz-Valckenberg, and M. Van Lookeren Campagne, "Geographic atrophy: clinical features and potential therapeutic approaches," Ophthalmology **121**(5), 1079–1091 (2014).
3. Z. Yehoshua, P. J. Rosenfeld, G. Gregori, and F. Penha, "Spectral domain optical coherence tomography imaging of dry age-related macular degeneration," Ophthalmic Surg Lasers Imaging **41**(6), 1373 (2010).
4. S. Schmitz-Valckenberg, C. K. Brinkmann, F. Alten, P. Herrmann, N. K. Stratmann, A. P. Göbel, M. Fleckenstein, M. Diller, G. J. Jaffe, and F. G. Holz, "Semiautomated image processing method for identification and quantification of geographic atrophy in age-related macular degeneration," Invest. Ophthalmol. Vis. Sci. **52**(10), 7640 (2011).
5. A. P. Göbel, M. Fleckenstein, S. Schmitz-Valckenberg, C. K. Brinkmann, and F. G. Holz, "Imaging geographic atrophy in age-related macular degeneration," Ophthalmologica **226**(4), 182–190 (2011).
6. A. S. Lindblad, P. C. Lloyd, T. E. Clemons, G. R. Gensler, F. L. Ferris, M. L. Klein, and J. R. Armstrong, "Change in area of geographic atrophy in the age-related eye disease study: AREDS report number 26," Arch. Ophthalmol. **127**(9), 1168–1174 (2009).
7. A. C. Bird, R. L. Phillips, and G. S. Hageman, "Geographic atrophy: a histopathological assessment," JAMA Ophthalmol. **132**(3), 338–345 (2014).
8. C. A. Curcio, J. D. Messinger, K. R. Sloan, A. Mitra, G. McGwin, and R. F. Spaide, "Human chorioretinal layer thicknesses measured in macula-wide, high-resolution histologic sections," Invest. Ophthalmol. Vis. Sci. **52**(7), 3943–3954 (2011).
9. B. J. Lujan, A. Roorda, R. W. Knighton, and J. Carroll, "Revealing Henle's fiber layer using spectral domain optical coherence tomography," Invest. Ophthalmol. Vis. Sci. **52**(3), 1486–1492 (2011).
10. B. J. Lujan, A. Roorda, J. A. Croskrey, A. M. Dubis, R. F. Cooper, J. K. Bayabo, J. L. Duncan, B. J. Antony, and J. Carroll, "Directional optical coherence tomography provides accurate outer nuclear layer and Henle fiber layer measurements," Retina **35**(8), 1511–1520 (2015).
11. T. Otani, Y. Yamaguchi, and S. Kishi, "Improved visualization of Henle fiber layer by changing the measurement beam angle on optical coherence tomography," Retina **31**(3), 497–501 (2011).
12. O. Carrasco-Zevallos, D. Nankivil, B. Keller, C. Viehland, B. J. Lujan, and J. A. Izatt, "Pupil tracking optical coherence tomography for precise control of pupil entry position," Biomed. Opt. Express **6**(9), 3405 (2015).
13. A. Wartak, M. Augustin, R. Haindl, F. Beer, M. Salas, M. Laslandes, B. Baumann, M. Pircher, and C. K. Hitzenberger, "Multi-directional optical coherence tomography for retinal imaging," Biomed. Opt. Express **8**(12), 5560 (2017).

14. . American National Standard Institute, Light Hazard Protection For Ophthalmic Instruments (ANSI Z80.36-2016) (2016).

15. A. Camino, P. Zang, A. Athwal, S. Ni, Y. Jia, D. Huang, and Y. Jian, "Sensorless adaptive-optics optical coherence tomographic angiography," Biomed. Opt. Express **11**(7), 3952–3967 (2020).

16. S. Ni, X. Wei, R. Ng, S. Ostmo, M. F. Chiang, D. Huang, Y. Jia, J. P. Campbell, and Y. Jian, "High-speed and widefield handheld swept-source OCT angiography with a VCSEL light source," Biomed. Opt. Express **12**(6), 3553 (2021).

17. Y. Jian, K. Wong, and M. V. Sarunic, "Graphics processing unit accelerated optical coherence tomography processing at megahertz axial scan rate and high resolution video rate volumetric rendering," J. Biomed. Opt. **18**(02), 1 (2013).

18. J. Xu, K. Wong, Y. Jian, and M. V. Sarunic, "Real-time acquisition and display of flow contrast using speckle variance optical coherence tomography in a graphics processing unit," J. Biomed. Opt. **19**(02), 1 (2014).

19. A. Camino, R. Ng, J. Huang, Y. Guo, S. Ni, Y. Jia, D. Huang, and Y. Jian, "Depth-resolved optimization of a real-time sensorless adaptive optics optical coherence tomography," Opt. Lett. **45**(9), 2612–2615 (2020).

20. M. D. Fischer, G. Huber, S. C. Beck, N. Tanimoto, R. Muehlfriedel, E. Fahl, C. Grimm, A. Wenzel, C. E. Remé, S. A. van de Pavert, J. Wijnholds, M. Pacal, R. Bremner, and M. W. Seeliger, "Noninvasive, in vivo assessment of mouse retinal structure using optical coherence tomography," PLoS One **4**(10), e7507 (2009).

21. R. C. Ryals, M. D. Andrews, S. Datta, A. S. Coyner, C. M. Fischer, Y. Wen, M. E. Pennesi, and T. J. McGill, "Long-term characterization of retinal degeneration in royal college of surgeons rats using spectral-domain optical coherence tomography," Invest. Ophthalmol. Vis. Sci. **58**(3), 1378 (2017).

22. A. E. Hendrickson and C. Yuodelis, "The morphological development of the human fovea," Ophthalmology **91**(6), 603–612 (1984).

23. X. R. Huang, R. W. Knighton, and L. N. Cavuoto, "Microtubule contribution to the reflectance of the retinal nerve fiber layer," Invest. Ophthalmol. Vis. Sci. **47**(12), 5363–5367 (2006).

24. T. Y. P. Chui, H. Song, C. A. Clark, J. A. Papay, S. A. Burns, and A. E. Elsner, "Cone photoreceptor packing density and the outer nuclear layer thickness in healthy subjects," Invest. Ophthalmol. Vis. Sci. **53**(7), 3545–3553 (2012).

25. D. C. Hood, M. A. Lazow, K. G. Locke, V. C. Greenstein, and D. G. Birch, "The transition zone between healthy and diseased retina in patients with retinitis pigmentosa," Invest. Ophthalmol. Vis. Sci. **52**(1), 101–108 (2011).

26. E. Terzibasi, M. Calamusa, E. Novelli, L. Domenici, E. Strettoi, and A. Cellerino, "Age-dependent remodelling of retinal circuitry," Neurobiol. Aging **30**(5), 819–828 (2009).

27. S. Gartner and P. Henkind, "Aging and degeneration of the human macula. I. outer nuclear layer and photoreceptors," Br. J. Ophthalmol. **65**(1), 23–28 (1981).

28. K. Eliasieh, L. C. Liets, and L. M. Chalupa, "Cellular reorganization in the human retina during normal aging," Invest. Ophthalmol. Vis. Sci. **48**(6), 2824–2830 (2007).

29. C. A. Curcio, N. E. Medeiros, and C. L. Millican, "Photoreceptor loss in age-related macular degeneration," Invest. Ophthalmol. Vis. Sci. **37**(7), 1236–1249 (1996).

30. G. Yiu, Z. Wang, C. Munevar, E. Tieu, B. Shibata, B. Wong, D. Cunefare, S. Farsiu, J. Roberts, and S. M. Thomasy, "Comparison of chorioretinal layers in rhesus macaques using spectral-domain optical coherence tomography and high-resolution histological sections," Exp. Eye Res. **168**(1), 69–76 (2018).

31. W. Gao, B. Cense, Y. Zhang, R. S. Jonnal, and D. T. Miller, "Measuring retinal contributions to the optical Stiles-Crawford effect with optical coherence tomography," Opt. Express **16**(9), 6486 (2008).

32. R. K. Meleppat, P. Zhang, M. J. Ju, S. K. Manna, Y. Jian, E. N. Pugh, and R. J. Zawadzki, "Directional optical coherence tomography reveals melanin concentration-dependent scattering properties of retinal pigment epithelium," J. Biomed. Opt. **24**(06), 1 (2019).

33. R. W. Knighton and C. Qian, "An optical model of the human retinal nerve fiber layer: Implications of directional reflectance for variability of clinical measurements," J. Glaucoma **9**(1), 56–62 (2000).

34. M. Draelos, P. Ortiz, R. Qian, C. Viehland, R. McNabb, K. Hauser, A. N. Kuo, and J. A. Izatt, "Contactless optical coherence tomography of the eyes of freestanding individuals with a robotic scanner," Nat. Biomed. Eng. **5**(7), 726–736 (2021).

35. S. Borkovkina, A. Camino, W. Janpongsri, M. V. Sarunic, and Y. Jian, "Real-time retinal layer segmentation of OCT volumes with GPU accelerated inferencing using a compressed, low-latency neural network," Biomed. Opt. Express **11**(7), 3968 (2020).